Journal of Magnetic Resonance 203 (2010) 150–155

Contents lists available at ScienceDirect

Journal of Magnetic Resonance

journal homepage: www.elsevier.com/locate/jmr

ESR micro-imaging of LiNc-BuO crystals in PDMS: Spatial and spectral grain distribution

Aharon Blank [a,*], Revital Halevy [a], Michael Shklyar [a], Lazar Shtirberg [a], Periannan Kuppusamy [b]

[a] Schulich Faculty of Chemistry, Technion – Israel Institute of Technology, Haifa 32000, Israel
[b] Center for Biomedical EPR Spectroscopy and Imaging, Davis Heart and Lung Research Institute, Department of Internal Medicine, The Ohio State University, Columbus, OH 43210, USA

ARTICLE INFO

Article history:
Received 29 October 2009
Revised 13 December 2009
Available online 22 December 2009

Keywords:
ESR
EPR
Microscopy
Imaging

ABSTRACT

Microcrystals of lithium octa-*n*-butoxynaphthalocyanine (LiNc-BuO) in a bio-compatible and oxygen-permeable polymer matrix of poly-dimethyl-siloxane (PDMS) can be used for repetitive non-invasive imaging of oxygen in live specimens by means of mm-scale electron spin resonance (ESR) imaging. This probe denoted as "*oxychip*" was characterized by high-resolution μm-scale ESR microcopy to reveal the fine details of its spatial and spectral properties. The ESR micro-images of a typical oxychip device showed that while the spatial distribution of the microcrystals in the polymer is fairly homogenous (as revealed by optical microscopy), the ESR signal originates only from a very few dominant crystals. Furthermore, spectral–spatial analysis in a microcrystal and a sub-microcrystal spatial resolution reveals that each crystal has a slightly different g-factor and also exhibits variations in linewidth, possibly due to the slightly different individual crystallization process.

© 2009 Elsevier Inc. All rights reserved.

1. Introduction

Electron spin resonance (ESR) is well known for its capability to quantify and image oxygen concentration in a variety of environments and biological systems [1]. In most cases a paramagnetic species, which is usually inserted into the system of interest, interacts with the paramagnetic oxygen molecule and experiences a reduction in its spin–spin relaxation time, T_2, in a linear proportionality to the oxygen concentration. Compared to other methods, such as Clarke electrodes, magnetic resonance imaging (MRI), positron emission tomography (PET), and optical-based methods (e.g., soluble phosphorescence probes or probes embedded in optical fibers), ESR oxymetry exhibits capabilities such as minimal tissue damage, reasonable accuracy and spatial resolution, reliability, repeatability, and real-time reporting of oxygenation/redox status of biological tissues without consumption of oxygen [2,3]. Furthermore, it is considered to be the only minimally-invasive technique that provides absolute values of oxygen concentration inside a tissue of interest [4], and can potentially be employed also for intracellular high-resolution oxygen mapping [5]. As noted above, since biological samples are mostly non-paramagnetic, appropriate spin probes must be placed or implanted within the tissue of interest in order to perform the ESR measurements. One of the main issues, limiting the use of ESR for these types of *in vivo* applications, is the potential toxicity and non-biocompatibility of the common ESR spin probes used for this purpose (e.g. trityl [6], lithium phthalocyanine (LiPc) [7], or lithium octa-*n*-butoxynaphthalocyanine (LiNc-BuO) [8]). One potential solution for these problems is by coating or encapsulation of the spin probes with a bio-compatible and oxygen-permeable material. Recently, this approach was implemented by encapsulation of LiNc-BuO crystal spin probes with poly-dimethyl-siloxane (PDMS) using a cast-molding and polymerization approach [9]. These microdevices, denoted as "oxychips", were thoroughly tested both in vitro and *in vivo* in terms of their spin distribution, surface properties, and oxygen response of T_2 [9,10].

Here we carry out a complementary analysis for the currently-available data, and provide high-resolution spatial and spectral ESR micro-images of typical oxychips. These images reveal the spin distribution at a resolution of ~30 μm, which is sufficient to identify and differentiate between the individual microcrystals that are embedded in PDMS. Furthermore, using this spatial resolution, spectral analysis of an oxychip was carried out on a microcrystal basis to investigate the sample heterogeneity in terms of signal strength (i.e. spin concentration for each crystal), crystal g-factor and linewidth. The results show that the optical image does not describe well the distribution of ESR signal strength among the embedded microcrystals, and that each microcrystal is characterized by slightly different g-factor and linewidth. Discussion of these finding is also given.

* Corresponding author. Address: Schulich Faculty of Chemistry, Technion – Israel Institute of Technology, Technion City, Haifa 32000, Israel. Fax: +972 4 829 5948.
E-mail address: ab359@tx.technion.ac.il (A. Blank).

1090-7807/$ - see front matter © 2009 Elsevier Inc. All rights reserved.
doi:10.1016/j.jmr.2009.12.011

2. Experimental details

The ESR micro-imaging experiments were carried out on a "home-built" ESR microscope recently developed at the Technion. A block diagram of the system is provided in Fig. 1A. The system is in principle based on the one developed at Cornell University [5,11], with some major changes and upgrades. These mainly include: (1) The use of a wideband "home-made" microwave bridge rather than a narrowband commercial system; (2) Imaging probe with improved heat dissipation properties; (3) Advanced data acquisition and processing software; and (4) Improved sample holders that enable the positioning of the sample in the center of the resonator. We shall first provide an overview of the system operational principles and then focus on some of its major components and add more details for them.

With reference to Fig. 1A, a standard PC (a) controls the system and is used for interfacing with the user via LabView data acquisition and analysis software. An analog output card (AO – model PCI-6733 from National Instruments) in the PC is used to tune the microwave (MW) frequency in the microwave bridge (g), determine the gradients pattern in the CW gradient driver unit (h) and provide reference modulation frequency to the lock-in amplifier (j). The MW signal coming out of the bridge goes into the imaging probe (l) and the reflected energy is amplified and detected back in the bridge. The signal then goes into a lock-in amplifier (Stanford Research System; model SR530) that is controlled via the RS232 interface of the PC (d). The signal continues back to the PC to an analog input card (AI, model PCI-6023 from National Instruments) for further processing. The imaging probe is located inside a standard 15" electromagnet (from Varian, model V3800), whose magnetic field is controlled via a combination of a Gaussmeter (Lakeshore model 475) and a home-made magnetic field controller unit (f) that drives local Helmholtz pair field bias coils (k) located in the electromagnet gap. The system supports the acquisition of 1-, 2-, 3-, or 4-D spatial and spectral–spatial ESR images via both the projection reconstruction and the modulated fields gradient methods [12]. The magnetic field is swept by the local gradient coils located in the imaging probe that also provide the modulation and field-frequency lock functionality to the system [11]. A frequency counter/power meter (item m in Fig. 1A; EIP model 545) is used to monitor the exact MW frequency and the power going into the resonator.

Following this general overview of the system, more details are provided on its key new components. The home-made CW microwave bridge is composed of three separate modules: An external power supply, an electronics module and a MW module. he electronics module includes several home-made cards that: (1) Provide control over the MW frequency and the MW power; (2) amplifies the detected MW signal; and (3) locks the MW frequency onto the resonance frequency of the resonator in the imaging probe (automatic frequency control – AFC). The MW module is constructed from discrete components and the basic schematic is shown in Fig. 1B. While all the MW components in the module can operate in the entire 6–18 GHz frequency range, the MW source has a limited tunability and has to be exchanged in order to work in different frequency regimes within this range. In the present system we employed a voltage-controlled oscillator (VCO) covering the 14.5–16 GHz frequency range as a MW source. The VCO is coupled to the electronic module which enables the AFC functionality of the bridge.

Another new and important component in the system is the CW gradient drive unit. This unit includes seven similar channels of current drivers, feeding the *X*-, *Y*- and *Z*-gradient coil pairs (two channels for each pair) and the modulation coils (used also for field-frequency-lock purpose). The drivers have a bandwidth of DC to ~150 kHz and a maximum current output drive of 3 A each. The drivers are based on an OPA544 amplifier with a feedback loop. The driver circuit also includes a zero bias compensation capability.

The third module of interest is the imaging probe, which is the heart of the system, providing its high sensitivity and fine image resolution. It is based on the pulsed ESR microscopy imaging probe

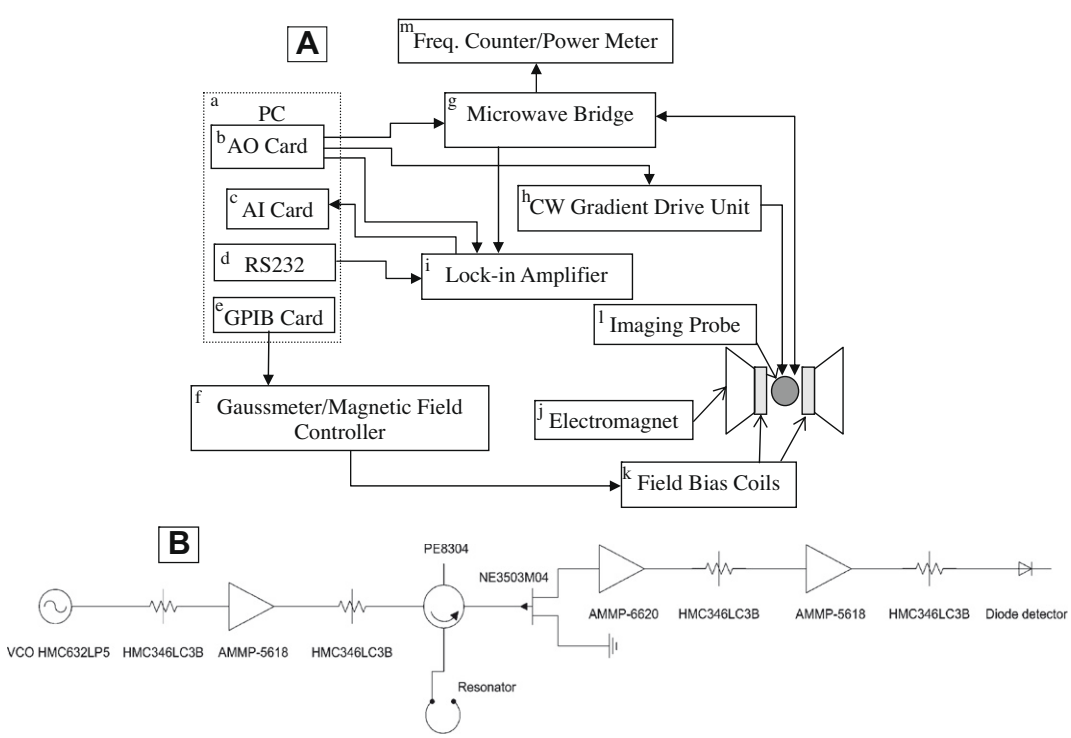

Fig. 1. (A) Block diagram of the CW ESR micro-imaging system; (B) Basic schematics of the microwave module in the CW ESR bridge.

described in details in [13] with some modifications in the gradient coil configuration and their cooling methodology. Thus, while the gradient coils geometry is identical to the one described in [13], each individual coil in a gradient-coil-pair is driven separately and therefore has different properties with respect to the gradient drivers. For example, each of the two *X*-gradient coils (based on Maxwell pair geometry) is exhibiting an inductance of 2.2 μH, a resistance of 1 Ω, and produces magnetic field gradient of 2.74 T/m·A (calculated via the method described in ref [14], assuming the coil counterpart is also fed by the same current magnitude). The Y-gradient coil is based on Golay geometry: each one of its two pars has a total inductance of 4.2 μH, a resistance of 1.1 Ω, and it produces magnetic gradient of 2.5 T/m·A. The Z-gradient coil is also based on Golay geometry and has an efficiency of 1.31 T/m·A. Each one of its two parts has an inductance of 4.45 μH and a resistance of 0.9 Ω. The maximum magnetic field gradient achieved by this system with the available 3 A current drive is ~8.2, 7.5, and 3.9 T/m, for the *X*, *Y*, and *Z* coils, respectively. However, in this work we confined ourselves to currents of up to ~1.8 A to avoid excessive coil and resonator heating. The gradient coils are embedded in heat-conductive adhesive, as detailed in [13], which effectively dissipates the heat away from the coils and prevents their destruction. However, since the resonance frequency of the Rutile crystal is very sensitive to the temperature (~10 MHz/K), efficient air flow had to be maintained all around the resonator to avoid sharp frequency changes that cause change of the optimal tuning/matching conditions and consequently signal reduction.

3. Sample preparation

The test sample with the LiPc and LiNc-BuO crystals was produced by placing two crystals of LiPc and one crystal of LiNc-BuO on a small (~1 mm in size) double-sided tape and then placing the tape in the glass sample holder. Details of LiNc-BuO particulate synthesis and fabrication methodology to obtain the LiNc-BuO PDMS chips were provided in ref [8,9]. A large piece (2 × 2 mm) of oxychip was sliced to a thickness of ~100 μm by sharp scalpel and then further cut to its final shape to fit into the imaging probe. All samples was sealed under argon atmosphere in a specially-prepared glass sample holder (prepared by the method described in Ref. [15]).

4. Results and discussion

At first, the sensitivity and imaging capability of the experimental system was examined with a test sample of LiPc and LiNc-BuO crystals (shown in Fig. 2A). The CW ESR spectrum of this sample, acquired with our system without any gradients, is given in Fig. 2B. The spin sensitivity of the system can be estimated by taking the approximate number of LiPc spins in our sample (~5×10^{13} spins, assuming LiPc has ~10^8 spins per $[1\ \mu m]^3$ [5,15]), and dividing it by the signal-to-noise-ratio (SNR) of the spectrum (312). It follows that under the experimental conditions detailed in Fig. 2B (averaging time of 0.1 s) the spin sensitivity is ~1.6×10^{11}. This sensitivity is almost two orders of magnitude worse than the expected optimal theoretical value (~1.6×10^9) [5], which is comparable to our results with similar probes in pulsed ESR [13]. This apparent discrepancy can be accounted for by several factors such as: (a) the sample was placed above and not inside the resonator (a factor of ~3 in sensitivity), (b) *Q* value was not optimized (~500 compared to 2000 in the theory – a factor of ~4 in sensitivity), and (c) the LiPc spin concentration may be lower than expected (unknown factor).

Following this the test sample was imaged by two types of imaging schemes, 2-D spatial and 2-D spatial 1-D spectral. The

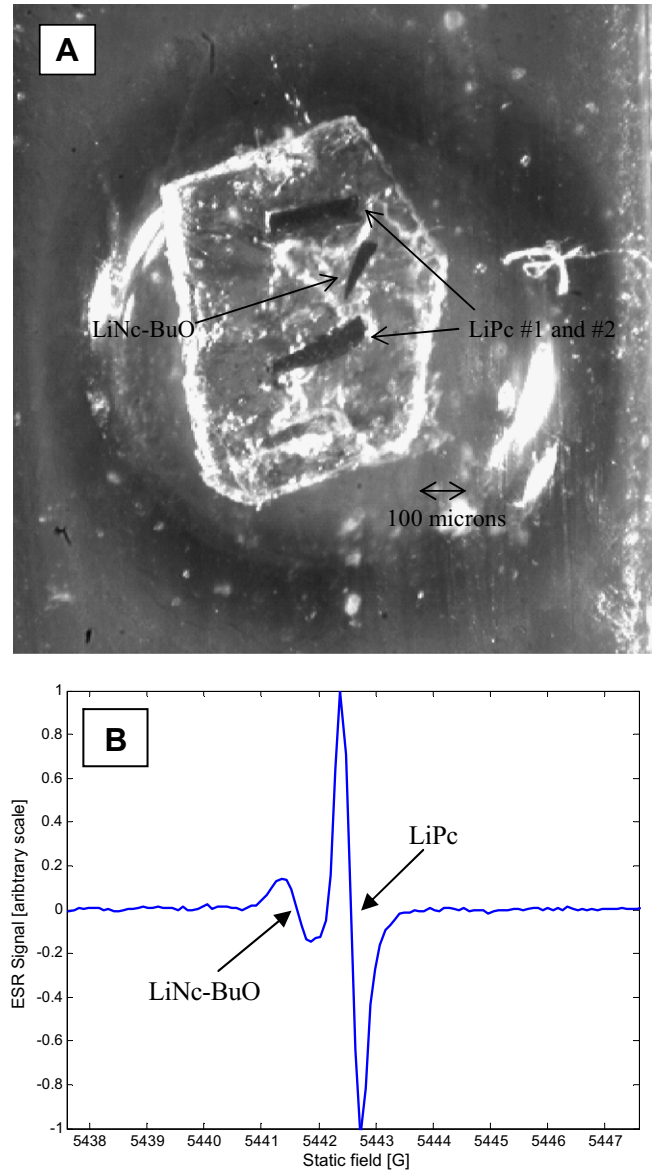

Fig. 2. (A) Optical image of the test samples used for the CW ESR microscope system evaluation; (B) CW ESR spectrum of the test sample. Experimental conditions were: Frequency 15.397 GHz, modulation amplitude 0.25 G, time constant for each spectrum point 0.1 s, sweep time 25.6 s.

2-D spatial image is shown in Fig. 3A. The field-frequency lock was fixed on the stronger LiPc signal and therefore the LiNc-BuO crystal, that has different g-factor, is smeared and appears as two crystals in this image. The image resolution can be estimated by the relation [5,12]:

$$\Delta x \approx \frac{2\Delta B_{1/2}}{G_x} \tag{1}$$

where $\Delta B_{1/2}$ is the ESR signal linewidth and G_x is the gradient magnitude. In our case, the LiPc signal was broadened by the field modulation to a linewidth of ~0.25 G and therefore the 2-D image resolution for the two LiPc crystals can be estimated to be ~10 μm. The image SNR can be found to be ~208. Furthermore, since the crystals diameter is ~30 μm (assuming rod-like crystal shape, typically 50–100 μm long), each voxel in the LiPc image (with dimensions of ~$10 \times 10 \times 30$ μm) contains ~3×10^{11} spins. Thus the spin sensitivity of the image can be estimated to be almost

$\sim 10^9$ spins (and this could be further optimized – see the sensitivity discussion above).

The results of the 2-D spatial 1-D spectral imaging measurements of the test sample are presented in Fig. 3C and D. It is apparent that one can obtain good distinction between the crystals, based on their spectral characteristics, while still maintaining the high-resolution of the image ($\sim$10 μm). Spatially-resolved ESR spectra characteristic to the LiPc and the LiNc-BuO crystals is shown in Fig. 3B. The two LiPc crystals exhibit very similar linewidth but slightly different g-factors. This may be due to g anisotropy (since they are not aligned in the same orientation) or other factors that will be discussed below in the context of the oxychip imaging. It should be also noted that the image resolution is good enough to have several voxels describing each microcrystal. Looking at all the available spectra for each microcrystal (not shown here) reveals that the spectra appearing in Fig. 3B are characteristic of each crystal, and no intra-crystal g-factor or linewidth variation were observed.

Following the system evaluation with the test sample, we have carried out 2-D spatial and 2-D spatial 1-D spectral imaging experiments with the LiNc-BuO in PDMS sample. An optical image of the sample is given in Fig. 4A. It is apparent that the sample contains many microcrystals with quite a wide range of sizes. A visual exam of the optical image shows that these crystals are distributed more or less in a homogenous manner with occasional clustering (which is difficult to see in Fig. 4A but is readily observable under the optical microscope). The ESR 2-D spatial image of this sample is shown in Fig. 4B. It is apparent that unlike the optical image, most of the signal originates from $\sim$6 to 7 dominant crystals, as marked in Fig. 4A. As shall be shown below, the linewidth and g-factor vary a bit from crystal to crystal, however, a nominal value for $\Delta B_{1/2}$ is $\sim$0.75 G. Thus, based on Eq. (1), the image resolution can be estimated to be $\sim$31 μm. The image SNR reaches a maximum of $\sim$90.

Following this, a spectral–spatial analysis was carried out for the most dominant seven crystals in the ESR image. The basic spectral parameters for each of these crystals are given in Table 1, and representative three spectra are shown in Fig. 5. Small variations in g-factor of up to 3×10^{-5} are observed. Furthermore, each crystal has slightly different linewidth, with variation of up to $\sim$20%. The variation in g may be due to either g anisotropy and/or slightly different microcrystal structures or crystal defects. Anisotropy in g is a well known phenomenon for single crystals and most probably

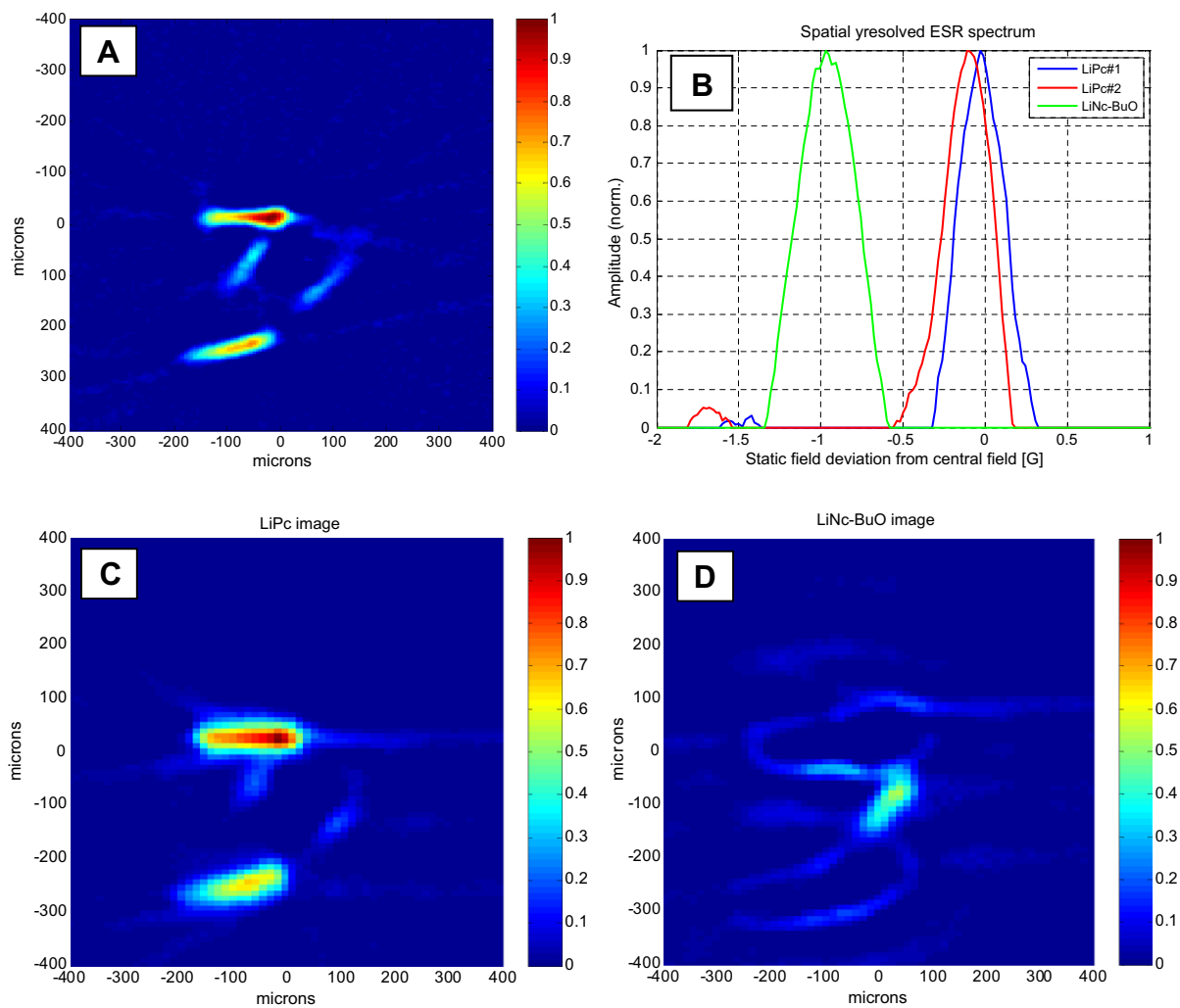

Fig. 3. (A) CW ESR image of the test sample shown in Fig. 2. A 2-D spatial image was acquired with 256 projections, time constant of 0.1 s and 256 points per projection. Modulation amplitude was 0.25 G and the gradient magnitude was 4.9, 4.5, and 2.3 T/m for the *X*-, *Y*-, and *Z*-axis, respectively. MW frequency was 15.397 GHz, center field was 5442.6 G and sweep range was 22 G. (B) Spatially-resolved ESR spectra for the LiPc and LiNc-BuO crystals obtained through spectral–spatial imaging of the test sample. Center field is 5442.6 G. The signals are normalized but their relative intensities can be obtained from images (C and D). (C) Spectral slice of the test sample with two LiPc and one LiNc-BuO crystal showing the signal that corresponds to the spectral peak of the LiPc crystals. (D) The same as (C) but just showing the signal that corresponds to the spectral peak of the LiNc-BuO crystal.

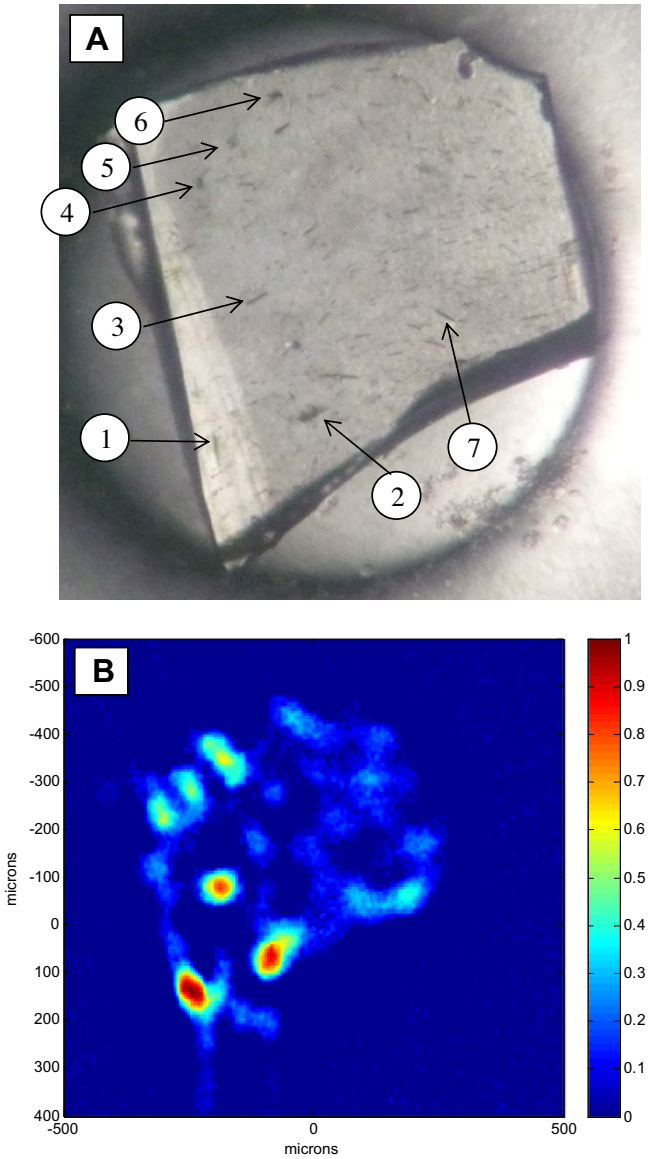

Fig. 4. (A) Optical image of the LiNc-BuO in PDMS sample with reference to specific crystals that exhibit stronger ESR signal than the others and were analyzed for their spectral properties. (B) CW ESR image of the oxychip sample. A 2-D spatial image was acquired with 256 projections, time constant of 0.1 s and 256 points per projection. Modulation amplitude was 0.7 G and the gradient magnitude was 4.9, 4.5, and 2.3 T/m for the *X*-, *Y*-, and *Z*-axis, respectively. MW frequency was 15.410 GHz, center field was 5447.2 G and sweep range was 22 G.

Table 1
Basic ESR spectral parameters for the seven most dominant crystals, in terms of the ESR signal. Location of the center of the spectral peak is given with respect to a central field of 5447.2 G.

Crystal #	Location of center (G)	Linewidth (G)
1	−0.165	0.709
2	−0.04	0.811
3	−0.045	0.732
4	−0.14	0.768
5	−0.11	0.852
6	−0.08	0.789
7	−0.03	0.880

exists also for LiNc-BuO (but was not measured yet). Variation of g due to different crystal structure or crystal defects was also observed in the past many times. For example, DPPH crystals

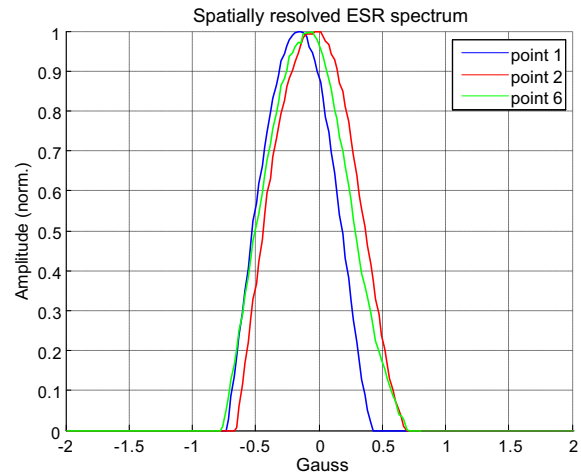

Fig. 5. ESR spectra for crystals # 1, 2, and 6, obtained through spectral–spatial imaging of the LiNc-BuO in PDMS sample. Center field is 5447.2 G. The signals are normalized but their relative intensities can be obtained from Fig. 4B.

may exhibit slightly different g-factors, depending upon the method with which they have been prepared [16]. As for the linewidth variations, they can be accounted for by either: (a) anisotropy in the relaxation rates; (b) slightly different non-optimal crystal structure (it is known that LiNc-BuO should be calibrated from batch to batch for its anoxic linewidth [17], so obviously crystal-to-crystal variations are also possible); or (c) possibly some of the signal peaks observed in the ESR image may be due to a cluster of crystals (for example, point 2), which, due to the g-factor variation phenomenon, can cause further signal broadening. Due to the relatively large modulation amplitude employed in the ESR image acquisition (0.7 G), it is expected that it will be difficult to observe anisotropy in the relaxation rate and therefore most probably the dominant effect here is crystal-to-crystal variation or crystal clustering.

5. Conclusions

A new CW ESR micro-imaging system was presented and tested. The system can produce images with resolution in the μm-scale (depending on the sample linewidth), which can be further analyzed to provide spatially-resolved spectral data. The system was utilized for the imaging of a typical "oxychip" sample and provided details regarding the spin distribution in the sample, which were found to be quite different from the optical image. Furthermore high-resolution spectral–spatial imaging revealed the spectral characteristics of individual microcrystal, which exhibit both g and line width variations. It can be concluded that optical data by itself is not enough and ESR microscopy should be used to verify the exact origin of the ESR signal in such type of samples. Moreover, when pO_2 is estimated through the linewidth measurement of a whole oxychip probe, one should consider the possible effects of linewidth variations and g anisotropy. Thus, for example, if a chip signal originates from just one or two dominate crystals the linewidth calibrations (usually taken on assemble of microcrystals) may not provide the correct oxygen response of the probe. Finally, while it was not the main intention of this work, the fact that the spectrum of many individual microcrystals can be acquired by the methodology we presented here may evolve to a new way of characterizing the g anisotropy of single crystals for which large signal crystals are difficult to or cannot be produced.

Acknowledgments

This work was partially supported by the US–Israel Binational Science Foundation (BSF) (Grant 2005258), the Israeli Science Foundation (Grants 169/05 and 1143/05), the European Research Council (ERC Grant #201665), NIH EB004031, and by the Russell Berrie Nanotechnology Institute at the Technion. We greatly thank Dr. Guruguhan Meenakshisundaram and Dr. Edward Eteshola (The Ohio State University) for preparation of the LiNc-BuO – PDMS samples. The help of Yael Talmon with the preparation of photolithographic glass sample holders is also greatly appreciated.

References

[1] H.M. Swartz, Measuring real levels of oxygen in vivo: opportunities and challenges, Biochem. Soc. Trans. 30 (2002) 248–252.
[2] R. Springett, H.M. Swartz, Measurements of oxygen in vivo: overview and perspectives on methods to measure oxygen within cells and tissues, Antioxid. Redox Signal. 9 (2007) 1295–1301.
[3] D.S. Vikram, J.L. Zweier, P. Kuppusamy, Methods for noninvasive imaging of tissue hypoxia, Antioxid. Redox Signal. 9 (2007) 1745–1756.
[4] N. Khan, B.B. Williams, H. Hou, H. Li, H.M. Swartz, Repetitive tissue pO_2 measurements by electron paramagnetic resonance oximetry: current status and future potential for experimental and clinical studies, Antioxid. Redox Signal. 9 (2007) 1169–1182.
[5] A. Blank, C.R. Dunnam, P.P. Borbat, J.H. Freed, High resolution electron spin resonance microscopy, J. Magn. Reson. 165 (2003) 116–127.
[6] J.H. Ardenkjaer-Larsen, I. Laursen, I. Leunbach, G. Ehnholm, L.G. Wistrand, J.S. Petersson, K. Golman, EPR and DNP properties of certain novel single electron contrast agents intended for oximetric imaging, J. Magn. Reson. 133 (1998) 1–12.
[7] K.J. Liu, P. Gast, M. Moussavi, S.W. Norby, N. Vahidi, T. Walczak, M. Wu, H.M. Swartz, Lithium phthalocyanine – a probe for electron-paramagnetic-resonance oximetry in viable biological-systems, Proc. Natl. Acad. Sci. USA 90 (1993) 5438–5442.
[8] R.P. Pandian, N.L. Parinandi, G. Ilangovan, J.L. Zweier, P. Kuppusamy, Novel particulate spin probe for targeted determination of oxygen in cells and tissues, Free Radic. Biol. Med. 35 (2003) 1138–1148.
[9] G. Meenakshisundaram, E. Eteshola, R.P. Pandian, A. Bratasz, S.C. Lee, P. Kuppusamy, Fabrication and physical evaluation of a polymer-encapsulated paramagnetic probe for biomedical oximetry, Biomed. Microdevices 11 (2009) 773–782.
[10] G. Meenakshisundaram, E. Eteshola, R.P. Pandian, A. Bratasz, K. Selvendiran, S.C. Lee, M.C. Krishna, H.M. Swartz, P. Kuppusamy, Oxygen sensitivity and biocompatibility of an implantable paramagnetic probe for repeated measurements of tissue oxygenation, Biomed. Microdevices 11 (2009) 817–826.
[11] A. Blank, C.R. Dunnam, P.P. Borbat, J.H. Freed, 3D Continuous wave electron spin resonance microscope, Rev. Sci. Instrum. 75 (2004) 3050–3061.
[12] G.R. Eaton, S.S. Eaton, K. Ohno, EPR Imaging and In vivo EPR, CRC Press, Boca Raton, 1991.
[13] A. Blank, E. Suhovoy, R. Halevy, L. Shtirberg, W. Harneit, ESR imaging in solid phase down to sub-micron resolution: methodology and applications, Phys. Chem. Chem. Phys. 11 (2009) 6689–6699.
[14] J.-M. Jin, Electromagnetic Analysis and Design in Magnetic Resonance Imaging, CRC Press, Boca Raton, 1999.
[15] K.J. Liu, G. Bacic, P.J. Hoopes, J.J. Jiang, H.K. Du, L.C. Ou, J.F. Dunn, H.M. Swartz, Assessment of cerebral pO_2 by EPR oximetry in rodents – effects of anesthesia, ischemia, and breathing gas, Brain Res. 685 (1995) 91–98.
[16] N.D. Yordanov, Is our knowledge about the chemical and physical properties of DPPH enough to consider it as a primary standard for quantitative EPR spectrometry, in: 4th International Workshop on Electron Magnetic Resonance of Disordered Systems (EMARDIS-95)/1st International Seminar on Applied EPR, Springer Verlag, Sofia, Bulgaria, 1995, pp. 339–350.
[17] R.P. Pandian, Y.-I. Kim, P.M. Woodward, J.L. Zweier, P.T. Manoharan, P. Kuppusamy, Open molecular framework in lithium octabutoxy-naphthalocyanine paramagnetic crystal: implications for the detection of oxygen and nitric oxide by EPR spectroscopy, J. Mater. Chem. 16 (2006) 3609–3618.